CrystEngComm

Room-Temperature Synthesis, Growth Mechanisms and Optical Properties of Organic-Inorganic Halide Perovskite $CH_3NH_3PbX_3$ (X= I, Br and Cl) Single Crystals

Journal:	*CrystEngComm*
Manuscript ID	CE-ART-11-2020-001690.R2
Article Type:	Paper
Date Submitted by the Author:	30-Mar-2021
Complete List of Authors:	Bari, Maryam; Simon Fraser University, Chemistry Wu, Hua; Donghua University, Applied Physics Bokov , Alexei; Simon Fraser University, Department of Chemistry and 4D LABS Ali, Rana Raryad; Simon Fraser University Tailor, Hamel; Simon Fraser University, Gates, Byron; Simon Fraser University, Department of Chemistry; Simon Fraser University Ye, Zuo-Guang; Simon Fraser University, Chemistry

ARTICLE

Room-Temperature Synthesis, Growth Mechanisms and Optical Properties of Organic-Inorganic Halide Perovskite $CH_3NH_3PbX_3$ (X= I, Br and Cl) Single Crystals

Received 00th January 20xx,
Accepted 00th January 20xx

DOI: 10.1039/x0xx00000x

Maryam Bari [a], Hua Wu [b,a], Alexei A. Bokov [a], Rana Faryad Ali [a], Hamel N. Tailor [a], Byron D. Gates [a], and Zuo-Guang Ye [a]*

Single crystals of the organic-inorganic halide perovskites are well needed in order to fully explore their potential in optoelectronic applications and to gain a fundamental understanding of their intrinsic properties. Previously, inverse temperature crystallization (ITC) was used to grow halide perovskite crystals at high temperatures (≈ 100 °C). Here, we develop an effective synthetic technique by which the $CH_3NH_3PbX_3$ (X= I, Br, and Cl) crystals are grown in polar solvents at room temperature (except for $CH_3NH_3PbI_3$ grown at 45 °C) in a relatively short time. A constant supersaturation during the crystal growth is created to produce large single crystals, which is achieved during room temperature crystallization (RTC) through controlled solvent evaporation. We investigate the effects of the temperature and supersaturation level on the nucleation kinetics of $CH_3NH_3PbCl_3$ as an example, and propose and compare the different growth pathways. The crystal structural analysis, steady-state absorption, photoluminescence, and charge-transport properties demonstrate excellent long-term stability (over 2 years) of the RTC-grown $CH_3NH_3PbX_3$ (X= Br, Cl) crystals against environmental degradation and moisture. The crystal optical properties are studied by polarized light microscopy, revealing birefringent ferroelastic domain structures characteristic of the tetragonal (X = Br) or orthorhombic (X = Cl) symmetry and high optical quality. This work presents a general strategy for designing, controlling, and optimizing the growth of high-quality halide perovskite crystals, which is an important step forward toward realizing high-end and stable optoelectronic devices such as nonlinear absorbers, photocatalyst, and micro-electromechanical actuators.

Introduction

Organic-inorganic halide perovskites have rapidly emerged at the forefront of photovoltaic devices exhibiting a power conversion efficiency of over 22% for the $CH_3NH_3PbI_3$ solar cells, with a relatively low cost and simple processing technique, [1-5] making them a serious competitor in commercial photovoltaics. As a part of the ABX_3 perovskite family, $MAPbX_3$ (MA = CH_3NH_3; X= I, Br and Cl) have shown unprecedented potential for the various single crystal (SC)-based devices such as photon,[6-9] X-ray[10] and gamma-ray detectors,[11] owing to their high photosensitivity and detectivity with fast response features. More recently, such perovskites were found to be high-performance nonlinear absorbers (e. g., $MAPbBr_3$ SC),[12,13] making them a viable alternative to silicon in optical communication and information processing,[14,16] and to exhibit a large electrostriction response (e. g., $MAPbI_3$ SC), potentially useful for such technologies as sonar transducers and micro-electromechanical systems.[17] For many applications, the use of halide perovskite SC with high purity and low defect concentrations could lead to enhanced device performance and stability over their polycrystalline counterparts.[18,19] These crystals also appear to be crucial for investigating the intrinsic nature of structural and photo-physical/chemical properties.[20-24]

So far, several approaches have been developed to grow halide perovskite crystals, including the solution temperature lowering (STL),[25-27] antisolvent vapor-assisted crystallization (AVC),[18] and inverse temperature crystallization (ITC) methods.[28,29] STL is a relatively simple process that involves cooling a preheated solution, e. g., a hydroiodic acid (HI) solution for the growth of $MAPbI_3$ SC.[30] Seed-assisted growth such as bottom-seeded solution growth (BSSG)[31] and top-seeded solution growth (TSSG)[32] techniques were applied to increase the size and quality of the crystals, in which a small crystal is used as seed, followed by the STL process. Large $MAPbI_3$ and $MASnI_3$ single crystals were obtained using these methods, but growing centimeter-sized crystal usually takes about one month.[30,32] On the other hand, the solubility of halide perovskites decreases with increasing temperature in certain polar solvents such as γ-butyrolactone (GBL), dimethyl sulfoxide (DMSO), and N, N-dimethylformamide (DMF). Based

[a] Department of Chemistry and 4D LABS, Simon Fraser University, Burnaby, British Columbia, V5A 1S6, Canada.
[b] Department of Applied Physics, Donghua University, Songjiang, Shanghai, 201620, China.
[c] *Corresponding Author. E-mail: zye@sfu.ca
Electronic Supplementary Information (ESI) available: [details of any supplementary information available should be included here]. See DOI: 10.1039/x0xx00000x

on this feature, ITC was designed to grow the $MAPbX_3$ (X = I, Br, and Cl) crystals at high temperatures over several hours.[7,28] ITC can produce large crystals (up to a two-inch size) by seed-induced heterogeneous nucleation approach,[33] which have been used to fabricate various devices of high performance, such as SC solar cells with a power conversion efficiency (PCE) ~ 21%[34] and SC photodetectors.[6,7]

High temperature (HT) growth may induce some invisible or visible defects such as inclusions, dislocations, strain, and growth steps in the crystals especially when the thermal gradient during the growth cannot be minimized, which may negatively impact their carrier properties, as evidenced in the literature with different values of carrier mobility and lifetime.[28,33,35] More recently, attention has been paid to the low temperature (LT) growth to improve the structural perfection, and a number of approaches have been developed such as low-temperature gradient crystallization (LTGC),[36] low temperature (45 °C) rapid crystallization,[37] room-temperature (RT) liquid-diffused separation induced crystallization (LDSC),[38] RT growth of $MAPbCl_3$,[39] and antisolvent assisted inverse temperature growth of $MAPbI_3$.[40] The LT-grown crystals exhibited better carrier performance (an increase by ~3 times in charge mobility and lifetime)[16,18,36] with the density of defect traps almost half of that of the HT-grown crystals.[36,38,39]

In terms of processing, the precursor solution typically needs to be replaced several times to obtain large crystals by ITC, which results in low efficiency and a time-consuming process.[33] This issue also appears in the LT growth methods by which it often takes several weeks to grow large crystals [16,36,39] with precise temperature control.[16,36] For instance, the $MAPbCl_3$ crystals of medium size were lately grown at RT by solvent evaporation in four weeks.[39]

Given the challenges of the currently used methods, it is necessary to develop a rapid and effective technique to grow the $MAPbX_3$ single crystals at room temperature, in order to meet the increasing demand for halide perovskite single crystals both for scientific investigations and device applications and to understand the complex growth mechanisms. In this work, we have successfully grown the $CH_3NH_3PbX_3$ crystals at room temperature (except for X = I at 45 °C) via controlled solvent evaporation. By this optimized room-temperature crystallization (RTC) process, a large quantity of the crystals of several millimeters in size can be grown in just several hours for X = I & Br, and a few days for X = Cl without the need for crystal seeding. More importantly, the first $MAPbBr_3$ and $MAPbCl_3$ crystals grown by RTC in 2018 demonstrate excellent long-term stability (over 2 years) against environmental degradation and moisture. In addition, the crystallization kinetics of $MAPbCl_3$ at room temperature and high temperature is investigated in detail. The solubility behaviour, induction time, interfacial energy, and some important nucleation parameters are determined. The absorption, photoluminescent (PL), and PL decay time properties and ferroelastic domain structures of the RTC-grown crystals are characterized. From the experimental results, the crystal growth mechanisms of $MAPbCl_3$ at 25 °C and 110 °C are proposed and compared. Based on this analysis, the factors controlling the size and quality of crystals are discussed, providing the optimum conditions for the RT growth of halide perovskite crystals.

Results and discussion

Crystal Growth of $MAPbX_3$, Structural Characterization, and Long-Term Stability. To grow the $MAPbX_3$ (X=I, Br and Cl) crystals, a saturated precursor solution was prepared, then cooled down and left at room temperature (at 45 °C for X = I) in a semi-closed vial for several hours (see the details in the Experimental Section). The solvents were selected based on their ability to dissolve both inorganic and organic halide precursors. Various combinations of solutes and solvents were examined, and the best results were obtained by dissolving CH_3NH_3X and PbX_2 (X = I, Br, and Cl) into GBL to grow $MAPbI_3$, into DMF to grow $MAPbBr_3$ and into DMSO to grow $MAPbCl_3$. The schematic diagrams of the RTC method along with the resultant crystals are presented in Fig. 1a-c. A large number of crystals were grown simultaneously (see Supporting Information, Fig. S1), and Fig. 1a shows a relatively large $MAPbI_3$ crystal that was grown in just 3 hours. Similarly, many transparent $MAPbBr_3$ crystals of orange colour with sizes between ~ 2 and 20 mm^3 were obtained at room temperature in less than 12 hours, as shown in Fig. 1b and Fig. 1S. Fig. 1c shows one of the grown $MAPbCl_3$ crystals with a size of ~ 4 mm^3 obtained by RTC after two days of growth. Interestingly, the crystals grew up to ~ 70 mm^3 after three more days, while maintaining good transparency.

The required supersaturation for RT crystallization was attained by controlled evaporation of the solvent, and the evaporation rate determines the growth time. The growth time for the $MAPbI_3$ and $MAPbBr_3$ crystals was much shorter than for $MAPbCl_3$, which could be due to strong coordination of DMSO with the halide perovskite, leading to slower evaporation of DMSO.[41,42] In addition, DMSO has a lower vapor pressure (~ 0.42 Torr) than DMF (~ 2.7 Torr) and GBL (~ 1.5 Torr) at room temperature,[42] which is also an important contributor to its lower solvent evaporation rate. To compare the RTC growth with the HT growth, we used ITC to grow the $MAPbCl_3$ crystals at high temperatures. A saturated solution of the precursors was prepared in DMSO at 60 °C and the solution was then heated to 110 °C in a fully closed vial over 12 hours. Due to the negative solubility of $MAPbCl_3$ in polar solvents such as DMSO,[7] a supersaturation was induced in the solution, leading to crystallization at 110 °C. Fig. 1d shows a sketch of the ITC process and selected large grown crystals [while many smaller (< 6 mm^3) crystals were formed in 12 hours]. Then, the seed-assisted method[33] was used to grow larger crystals. In this process, a good spontaneously grown crystal was selected as the nucleation seed and placed into a fresh precursor solution at 110 °C for an additional 12 hours to form a larger crystal (Fig. 1d). Our results confirm the literature reports that the ITC method is a fast-growing process which can lead to high-quality small to medium size crystals[7,33,37,43] and that, generally, the transparency of the HT-grown crystal drops in the second run of (seeded) growth as the crystal size increases. In terms of yield, with no need for seeding, the RTC technique results in yields of ~40 wt%, 60 wt% and 15 wt% for

X = I, Br, and Cl, respectively, making it a more efficient and cost-effective method compared to the HT growth with the yields of 5 wt% for $MAPbCl_3$ from this work, and 11 wt% and 35 wt% for X= I and Br, respectively, according to a previous report.[28]

Fig. 1e-g shows the powder and single-crystal X-ray diffraction patterns of the halide perovskite crystals grown using the RTC method. As displayed in the lower panels of Fig. 1e-g, the results of a Pawley refinement analysis confirmed the formation of a perovskite structure with a cubic symmetry ($Pm\bar{3}m$ space group) for the $MAPbBr_3$ and $MAPbCl_3$ crystals and a tetragonal symmetry ($I4/mcm$ space group) for the $MAPbI_3$ crystals. These refinements yield the lattice parameters of a = 5.665 Å and 5.918 Å for $MAPbCl_3$ and $MAPbBr_3$, respectively, and a = 8.877 Å and c = 12.628 Å for $MAPbI_3$, consistent with previously reported data.[26] Furthermore, the single-crystal XRD patterns of the as-grown $MAPbCl_3$ and $MAPbBr_3$ crystals show the presence of the (100), (200), (300), and (400) peaks with strong diffraction intensities, indicating that the naturally developed facets of the crystals belong to the {h00} planes (Upper panels of Fig. 1f and 1g). The $MAPbI_3$ crystal shows sharp peaks of (112) and (224), belonging to the {112} plane of the tetragonal structure (Upper panel of Fig. 1e). The full width at half maximum (FWHM) of the first two peaks was calculated for $MAPbX_3$ (X = I, Br, and Cl). The FWHM values of the (112) and (224) peaks are 0.040° and 0.045°, respectively, for $MAPbI_3$. The FWHM values of the (100) and (200) peaks are 0.026° and 0.031° for $MAPbBr_3$, and 0.034° and 0.039° for $MAPbCl_3$, respectively. These values are in the narrow range of ~ 0.026° - 0.045°, indicating that the RTC-grown single crystals are well-orientated and of good crystallinity, comparable to the quality of the $MAPbX_3$ crystals reported in the literature.[36,38,43]" Fig. S2 shows the result of energy-dispersive X-ray spectroscopy (EDX) analyses obtained from the $MAPbX_3$ crystals. The Pb: X ratio averaged from several EDX experiments at different points on a crystal surface is found to be 1: 3 ($\pm$ 0.06), in close agreement with the nominal composition of the perovskite phase.

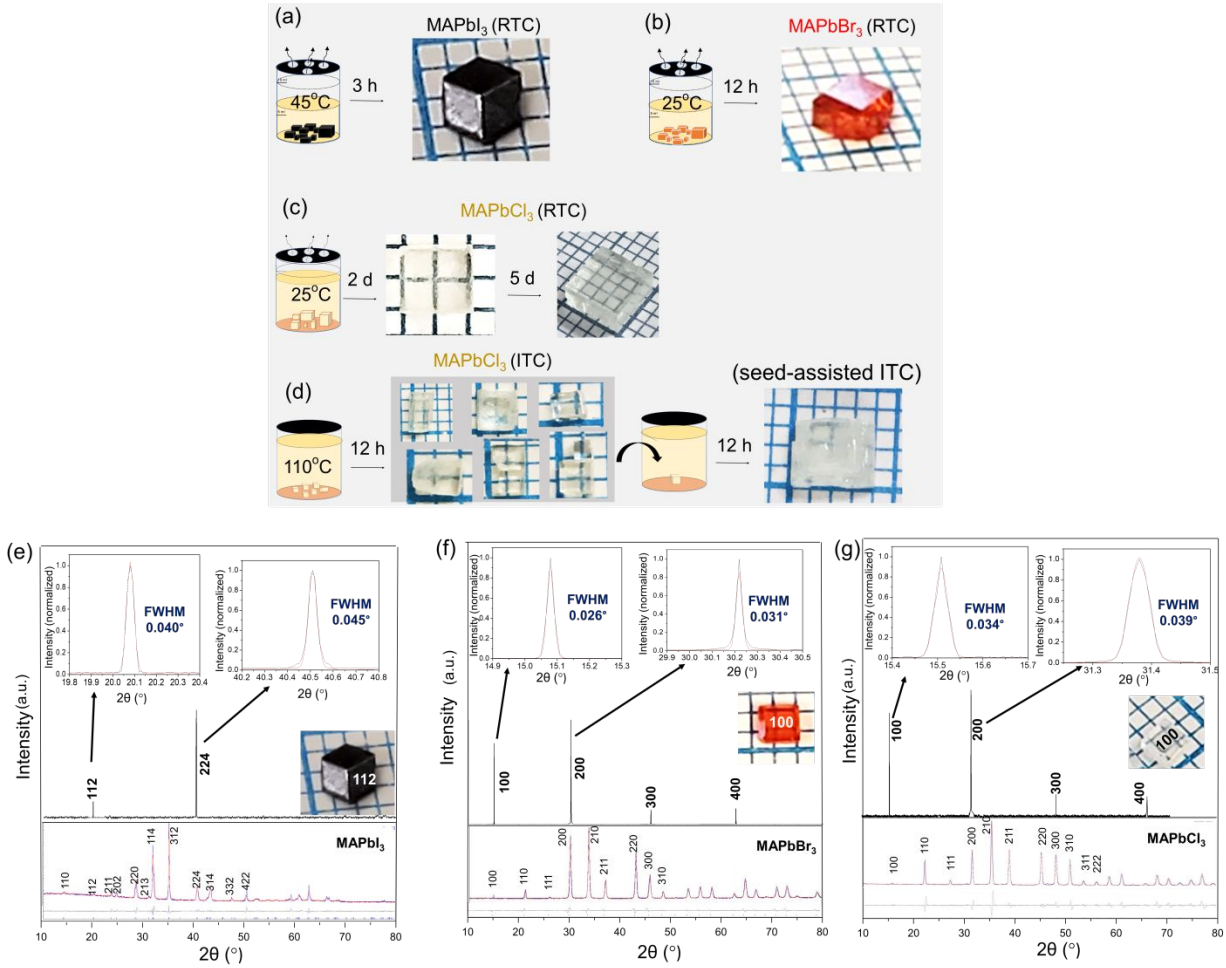

Fig. 1 Results of $MAPbX_3$ Crystal Growth and Structural Characterization. (a-c) Schematics of the room temperature crystallization (RTC) method and the examples of grown $MAPbI_3$ (a), $MAPbBr_3$ (b) and $MAPbCl_3$ (c) crystals. (d) Schematics of the inverse temperature crystallization (ITC) method and the grown $MAPbCl_3$ crystals, without and with seed-assisted growth. (e-g) Lower panels: Powder X-ray diffraction patterns of the $MAPbX_3$ (X= I, Br and Cl) crystals grown by the RTC method (blue line), the Pawley refinements (red line) with the profile residual factor R_{wp} = 0.56, 0.58, and 2.01 for $MAPbI_3$, $MAPbBr_3$, and $MAPbCl_3$, respectively, and the difference (grey line on the bottom of the panel). (e-g) Middle & Upper panels: Single crystal XRD patterns of the bulk $MAPbX_3$ (X =I, Br, and Cl) crystals grown via RTC (Insets), along with the high-resolution XRD patterns of the (112) and (224) diffraction peaks of $MAPbI_3$ and the (001) and (002) diffraction peaks of $MAPbBr_3$ and $MAPbCl_3$.

The long-term stability of the crystals, grown by RTC more than two years earlier, against environmental degradation and moisture was also investigated and no decomposition was observed from the PXRD patterns of the $MAPbX_3$ (X = Br, Cl) crystals, indicating that no degradation had happened over that period of time. These crystals have fully preserved their crystal structure, phase, morphology, and transparency (Fig. S3). However, the PXRD pattern of the $MAPbI_3$ crystals, which were grown a year earlier, shows some additional peaks corresponding to the yellow layer formed on the surface, which was identified to be $(CH_3NH_3)4PbI_6 \bullet 2H_2O$ (Fig. S4). As reported previously, the $MAPbI_3$ crystals can absorb ambient moisture to form a hydrate phase such as $(CH_3NH_3)4PbI_6 \bullet 2H_2O$.[44] Note that the crystals were not stored in a sealed dry condition but rather kept in an ordinary container in ambient condition.

Solubility and Supersaturation Studies. Our experiments demonstrate that the halide perovskite crystals can be grown in polar solvents at room temperature via solvent evaporation. To explain the RT and HT crystallizations of halide perovskites, it is necessary to understand the underlying mechanisms involved in the processes, which are closely related to saturation and solubility behaviour. Since the supersaturation is the main driving force for crystallization from solution, determining the optimum supersaturation is crucial for the RT growth of $MAPbX_3$, and it can be achieved by manipulating temperature, solution concentration, and solvent evaporation. The solubility limit as a function of temperature enables us to find the supersaturation at different temperatures. The solubility of $MAPbX_3$ in polar solvents was determined by measuring the equilibrium concentration (C^*) between 25 °C and 120 °C, as shown in Fig. 2a-c. The actual precursor concentration (C) for the prepared solutions of $MAPbI_3$, $MAPbBr_3$, and $MAPbCl_3$ is 6.2 g/mL, 7.2 g/mL, and 7.0 g/mL, respectively (as marked by the red dashed lines in Figure 2.a-c). The solubility of $MAPbI_3$ and $MAPbCl_3$ increases linearly with increasing temperature from 25 °C to 60 °C, followed by a decrease from 60 °C to 120 °C. The inverse solubility between 60 °C to 110 °C results in, upon heating, a decrease by 11% and 30% in the solubility of X = I and Cl in the solvent, respectively. This is equivalent to the creation of 11% (for X = I) and 30% (for X = Cl) supersaturation due to solubility reduction (S_{sr}). In contrast, the normal solubility behaviour existing between 60 °C and 25 °C results in, upon cooling, a solubility reduction by 11% (for X = I) and 12.5% (for X = Cl), giving rise to the corresponding supersaturation (S_{sr}). The $MAPbBr_3$ shows an absolute inverse solubility, as its solubility decreases monotonically with increasing temperature (Fig. 2b). While the supersaturation at high temperatures due to the negative solubility trend explains the principle of ITC, the supersaturation at 25 °C suggests that it is possible to grow the $MAPbI_3$ and $MAPbCl_3$ crystals at room temperature, justifying the feasibility of the RTC method. To test this hypothesis, we first cooled a saturated solution of X = I and Cl from 60 °C to 25 °C in a fully sealed vial and kept it at room temperature for several hours. No crystals were obtained for X = Cl. Some yellowish crystals were formed at the bottom of the flask containing the X = I solution, which were found to be an intermediate product of $(MA)_8[Pb_{18}I_{44}]$ from the Pawley refinement of the PXRD pattern. This result is consistent with the intermediate adduct of perovskite precursors and GBL precipitated at RT, as previously found (Fig. S5).[45] To avoid the undesired formation of the adduct, the growth temperature of $MAPbI_3$ was adjusted to 45°C.

This observation also shows that the 12.5% supersaturation was insufficient to trigger nucleation of $MAPbCl_3$ crystals at RT. Thus, an additional approach must be taken to increase supersaturation at room temperature, namely by solvent evaporation, which was also applied for X = Br and X= I (at 45 °C). The solutions were then transferred to a half-closed cap vial to allow the solvent to evaporate to produce more supersaturation (Fig. 1a-c). Various solvent evaporation conditions were investigated in which 0, 25, 50, 75, and 100 % of vial cap was closed and the optimum crystal growth was achieved using a vial with a half (50%)-closed cap (a 50 mL vial was used with a surface area of ~16 cm^2) for X = Br and Cl, and fully open vial for X = I. We further calculated the total (optimal) supersaturation (S_{total}) in our experimental conditions by combining the three different contributions to the supersaturation, i.e., $S_{total} = S_{sr} + S_{se} + S_{cg}$, where S_{sr} corresponds to the solubility reduction (Fig. 2a-c), S_{se} results from the solvent evaporation and S_{cg} is the negative supersaturation arising from crystal growth due to the decrease in solute concentration (see the detailed calculations in the Experimental Section). All the three individual factors (S_{sr}, S_{se}, and S_{cg}) together with the total supersaturation (S_{total}) were calculated versus growth time as shown in Fig. 2d-f. For example, S_{total} of $MAPbCl_3$ increases above 12.5 % at the early stage due to solvent evaporation, leading to nucleation and growth. As the growth proceeds, S_{total} reaches a value of 16 % after 2 days and maintains that level until day 5, providing an optimum window for the growth of $MAPbCl_3$ crystals at room temperature. The growth process slows down after five days when the total supersaturation drops to 11 % due to the formation of the crystals (Fig. 2f). Similar work was carried out for $MAPbBr_3$ and $MAPbI_3$ to find the desirable supersaturation for the RT growth, from which S_{total} was measured to be 13 % and 12 % for X = Br and I, respectively. It takes 2 h and 3 h for the nucleation onset to occur, and the growth process slows down after 12 h and 6 h for X = Br and I, respectively. For $MAPbI_3$, the actual concentration (C) of the solution (0.62 gr/mL) is lower than the equilibrium concentration ($C^* \approx 0.83$ gr/mL) at the growth temperature of 45 °C (marked by the red arrow in Fig. 2a), implying that solvent evaporation is needed first to compensate for the negative solubility reduction ($S_{sr} \approx -25\%$), and then to produce supersaturation for crystallization (Fig. 2d). $MAPbBr_3$ has retrograde solubility behaviour in the DMF solvent (Fig. 2b), and no S_{sr} exists at room temperature, hence, S_{total} is the sum of S_{se} and S_{cg} (Fig. 2e).

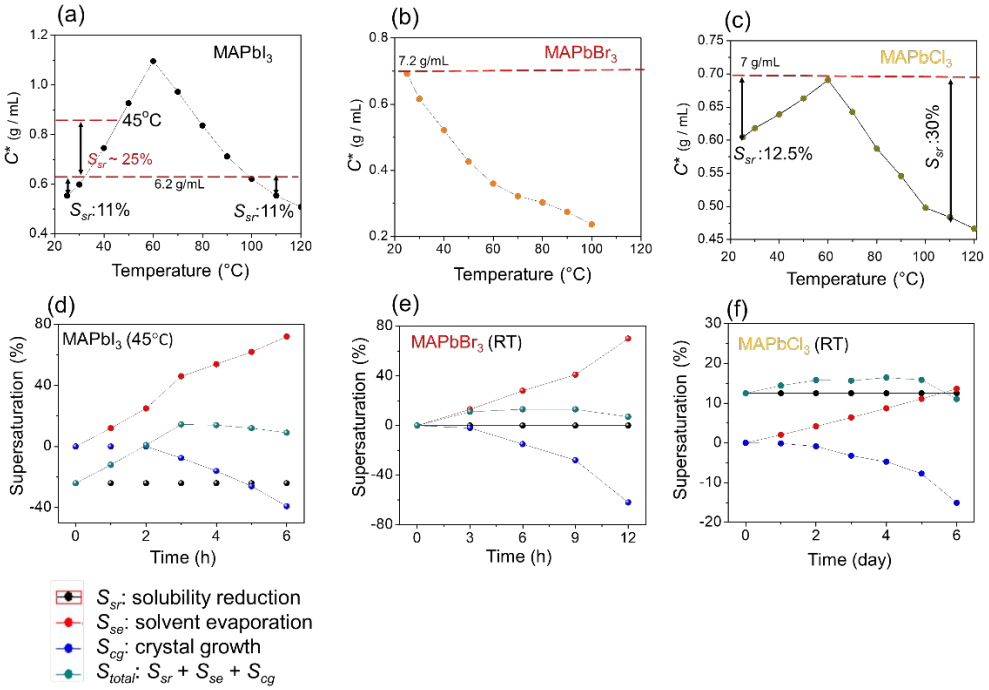

Fig. 2 Solubility curves of (a) $MAPbI_3$ in GBL, (b) $MAPbBr_3$ in DMF, (c) $MAPbCl_3$ in DMSO: Equilibrium concentration (C^*) as a function of temperature. The supersaturation created in the solution versus growth time: (d) $MAPbI_3$ at 45 ^{0}C, (e) $MAPbBr_3$ at RT, and (f) $MAPbCl_3$ at RT. Three factors contribute to the total supersaturation (S_{total}), i.e. solubility reduction (S_{sr}), solvent evaporation (S_{se}), and crystal growth (S_{cg}), resulting in a nearly constant total supersaturation (green curve) during the period of stable crystal growth.

Nucleation Mechanisms of $MAPbCl_3$ in RTC & ITC. As shown in Fig. 1c & 1d, the size of the grown crystals can be affected by the growth temperature. Here, we use classical homogeneous nucleation theory[46] to deduce the nucleation kinetics of the $MAPbCl_3$ crystals at 25 °C by RTC and 110 °C by ITC.

According to the classical nucleation theory, the relation between the induction time and the supersaturation ratio can be expressed as:[47,48]

$$\ln \tau = \mathrm{K} + \frac{16\pi\sigma^3 V_m^2 N_A}{3R^3T^3(\ln S_r)^2} \quad , \qquad (1)$$

where τ is the induction time, K is a constant, σ is the interfacial energy, V_m is the molar volume (= M/ρ, with M being the molar mass and ρ the density of $MAPbCl_3$), N_A is the Avogadro's number, R is the universal gas constant, S_r is the supersaturation ratio ($S_r = C/C^*$ with C being the actual concentration and C^* the equilibrium concentration), and T is the temperature. The induction time (τ), the time required for the crystallization of critical nuclei with a detectable size is important for evaluating the nucleation kinetics in this work. The experimental values of the induction time were measured at various supersaturation ratios (S_r) at two different temperatures (25 °C & 110 °C) and are plotted in Fig. 3a. At a given temperature, τ decreases with increasing supersaturation ratio. τ is found to be 300 minutes at the maximum S_r (= 1.15) at 25 °C, while only 103 minutes at the maximum S_r (= 1.44) at 110 °CAccording to Equation 1, a small τ value was obtained by ITC, favouring a fast crystal nucleation.

In the RTC process, it is believed that several precursor-solvent complexes are formed, which cannot be easily dissociated at room temperature (to be discussed in detail in the following section). Thus, the solubility reduction (supersaturation) is small, leading to a slower nucleation process and a longer induction time. Figure 3b shows the ln τ versus $1/(\ln S_r)^2$ plots of $MAPbCl_3$ at 25 °C and 110 °C, where the dashed lines are the least-square linear fittings of the experimental data. K and V_m in Equation 1 can be considered as constants. Then, the interfacial energy σ of the crystal can be calculated using the following equation:

$$\sigma = RT\left(\frac{3m}{16\pi V m^2 N_A}\right)^{\frac{1}{3}} \quad , \qquad (2)$$

when m is the slope of the linear fitting between ln τ and $1/(\ln S_r)^2$. As shown in Fig. 3b, the linear behaviour of ln τ versus $1/(\ln S_r)^2$ consists of two segments with different slopes, indicating two different nucleation mechanisms in the respective supersaturation regions. The higher supersaturation region (lower $1/(\ln S_r)^2$) in Fig. 3b with a steeper linear slope corresponds to a homogeneous nucleation, while the shallower linear relation in the lower supersaturation region (higher $1/(\ln S_r)^2$) indicates a heterogeneous nucleation. The interfacial energy of the homogeneous nucleation was calculated by using the steeper slope of the linear fitting, and it is found to be 2.5 mJ/m^2 for the RTC process and only 1.7 mJ/m^2 for the ITC one. These interfacial energy values agree well with the values reported for the growth of other organic compounds.[48,49] The smaller value in ITC implies a lower

interfacial energy needed for nucleation and consequently the formation of more nuclei with small sizes at high.

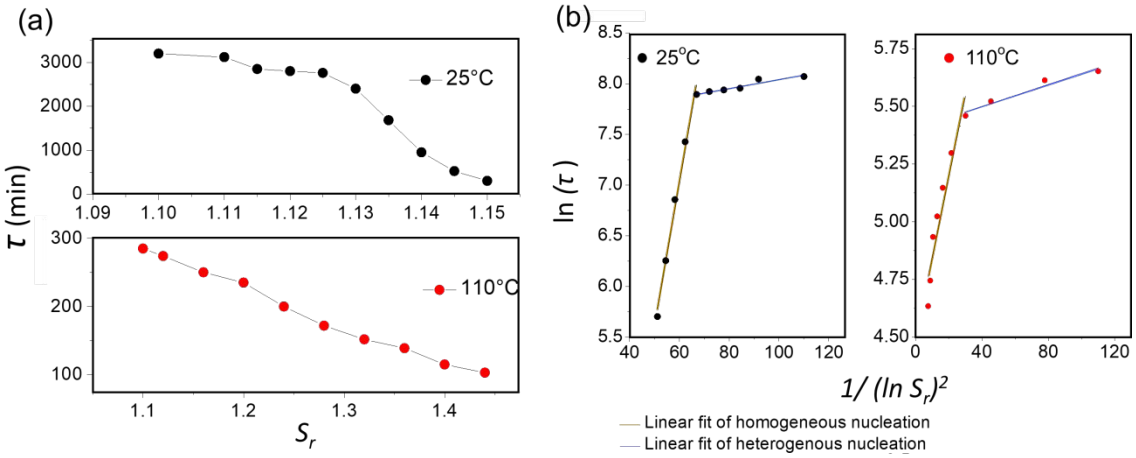

Fig. 3 Nucleation mechanisms of $MAPbCl_3$. (a) Dependence of induction time as a function of supersaturation for the $MAPbCl_3$ crystals at 25 °C and 110 °C. (b) Plots of ln (τ) versus $1/(\ln S_r)^2$; the slopes of the plots are used to calculate the interfacial energy of $MAPbCl_3$ at 25 °C and 110 °C, respectively.

temperatures. Based on the homogeneous nucleation theory, the nucleation parameters for 25 °C and 110 °C, such as the critical radius of nuclei (r_c), the Gibbs free energy per volume unit (ΔG_v), and the critical free energy barrier (ΔG_c) as a function of supersaturation, were calculated and the results are listed in Table 1 (detailed calculations of these parameters are provided in the Supporting Information). According to Table 1, ΔG_c decreases with the increase of supersaturation, and the ΔG_c values at 110°C are much smaller than those at 25 °C, indicating that the temperature and the supersaturation are two main factors that determine the crystal nucleation process. The critical radius of the nucleus (r_c) of the $MAPbCl_3$ crystals as a function of supersaturation is plotted in Figure S6. It can be seen that the r_c values at 110 °C are significantly smaller than those at 25 °C, which indicates that the higher temperature and the resultant higher supersaturation favour a decrease in the interfacial energy and the critical free energy barrier, leading to easier nucleation and smaller critical nuclei. In RTC, the large critical energy barrier allows only the crystals with nucleus radii larger than the critical one to grow, limiting the number of nuclei. Consequently, only a few large crystals are formed. These calculations and analysis are in good agreement with our experimental observations of the crystal growth by RTC and ITC (see Fig. 1c & d), respectively.

Growth Mechanisms of $MAPbCl_3$ by ITC and RTC. The analysis of the nucleation process allows us to deduce the growth mechanisms of $MAPbCl_3$ at high temperatures (ITC) and atroom temperature (RTC), and to determine the factors influencing the quality, quantity, and size of the grown crystals. Figure 4a and 4b depicts the growth mechanisms for ITC and RTC, respectively. In ITC (Fig. 4a), in the initial stage (I), the precursor solution prepared at 60 °C may contain two types of ions: the solute ions of Pb^{2+}, Cl^- and MA^+ and the precursor-solvent complex ions such as $PbCl_3^-$ and $[PbCl_3((CH_3)_2SO_3]^-$ similar to the PbI_2-DMSO complexes,[41,50] or iodoplumbate complexes.[51] The stability of the complex ions in the solution depends on temperature, precursor/solvent ratio, additives, and solvent strength. [37,52] Several studies reported that DMSO has a strong coordination affinity with solute ions, leading to the formation of stable complex ions.[41,42,53]

Table 1. Interfacial energy (σ) and nucleation parameters (the critical radius of the nuclei r_c, the Gibbs free energy per volume unit ΔG_v, and the critical free energy barrier ΔG_c) for the growth of $MAPbCl_3$ crystals with different supersaturation ratios (S_r) at 25 °C and 110 °C.

Temperature (°C)	S_r	σ (mJ/m²)	ΔG_v (×10⁶ J/m³)	r_c (nm)	ΔG_c (×10⁻²⁰J)
25	1.100	2.5	1.81	2.76	7.93
	1.110		1.99	2.52	6.62
	1.115		2.07	2.41	6.08
	1.120		2.16	2.32	5.61
	1.125		2.24	2.23	5.20
	1.130		2.33	2.15	4.83
	1.135		2.41	2.07	4.49
	1.140		2.49	2.00	4.20
	1.145		2.58	1.94	3.93
	1.150		2.66	1.88	3.69
110	1.100	1.7	2.33	1.46	1.51
	1.120		2.77	1.23	1.07
	1.160		3.63	0.94	0.62
	1.200		4.46	0.76	0.41
	1.240		5.26	0.65	0.30
	1.280		6.04	0.56	0.23
	1.320		6.79	0.50	0.18
	1.360		7.52	0.45	0.15
	1.400		8.23	0.41	0.12
	1.440		8.92	0.38	0.10

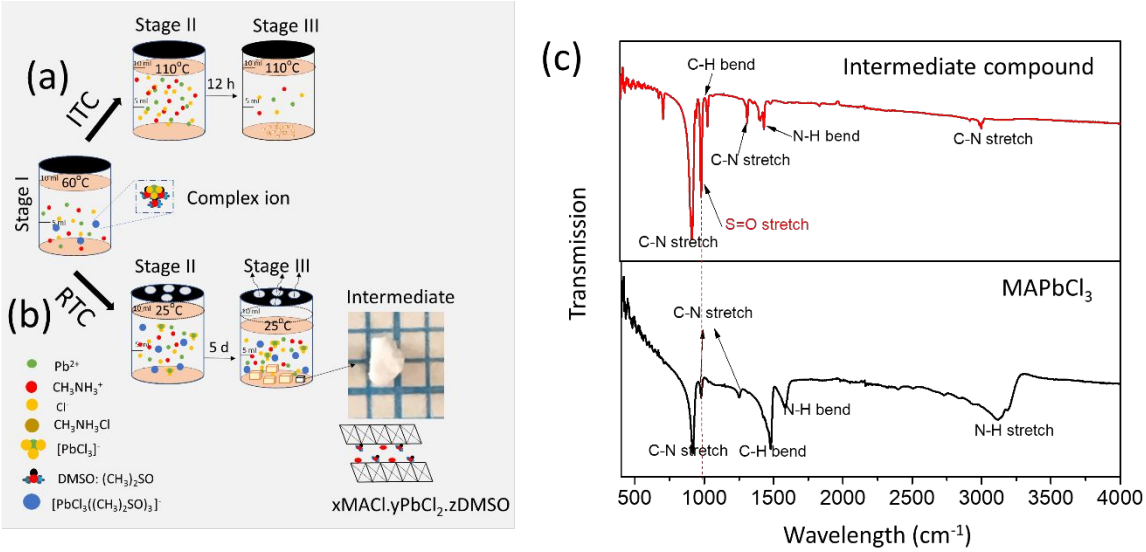

Fig. 4 Crystal growth mechanisms of $MAPbCl_3$ via (a) ITC and (b) RTC. Three stages are illustrated. Initial Stage (I): Preparation of a saturated solution at 60 °C; Intermediate Stage (II): Supersaturated state for both RTC (25 °C) and ITC (110 °C) before the nucleation process begins; and Final Stage (III): The solution in ITC is no longer supersaturated after a short duration of growth, while the one in RTC maintains its supersaturation. An intermediate compound was formed from the $xMACl.yPbCl_2.zDMSO$ system during the RTC growth. (C) IR spectra of $MAPbCl_3$ and the intermediate compound formed by the RTC method.

With the increase of temperature from 60 °C to 110 °C in ITC, the ionic complexes can extensively dissolve into the solution and produce a high concentration of ions (Intermediate Stage (II) in Fig. 4a), resulting in a high supersaturation, and hence a lowered interfacial energy and enhanced nucleation. By abruptly inducing a large supersaturation at a high temperature, many small crystals are formed quickly, accompanied by a decrease in the solute concentration (Final Stage (III) in Fig. 4a). The lowered concentration of solute ions prevents the crystals from growing to larger dimensions via spontaneous crystallization from the solution, which is no longer supersaturated. Therefore, to grow large crystals by ITC, it is necessary to use seed-assisted growth in which a high-quality pre-grown crystal is placed in a fresh supersaturated solution to grow further. In contrast, in the RTC process, by cooling from 60 °C to room temperature (Fig. 4b), the complexes do not dissociate as much as they do at high temperatures since the thermal energy is insufficient to break down completely the strong coordination bonds between DMSO and the precursor ions (Intermediate Stage (II) in Fig. 4b). Thus, the concentration of the precursor ions is lower in the solution at room temperature, which leads to larger interfacial energy, a small number of nuclei, and thereby larger crystals. To confirm the presence of the complex ions, the PXRD and infrared spectroscopy (IR) were performed on an intermediate compound, which was formed during the RTC process in the form of white crystals (Final Stage in Fig. 4b). The PXRD pattern shows that it is neither the $MAPbCl_3$ perovskite nor any of the precursor compounds (Fig. S7). The IR spectrum shown in Fig. 4c, together with that of $MAPbCl_3$ crystal, shows the characteristics of S=O stretching vibrations at 982 cm^{-1}, which confirm the presence of DMSO molecule in the intermediate compound. Although the exact composition of the intermediate compound cannot be determined reliably, it could be an intermediate product of the $xMACl\text{-}yPbCl_2.zDMSO$ system according to IR spectra. The stretching vibration of S=O for DMSO that normally appears at ~ 1045 cm^{-1} is shifted to 980 cm^{-1}, indicating the bond strength between sulfur and oxygen is decreased due to the formation of a new bond between DMSO and the $PbCl_2$ precursor.[54,55]

The above analysis indirectly confirms the presence of those complex ions in the solution. The term "colloid" was previously used and it was shown that the colloid contains Pb^{2+} and halide ions, which can be broken down by increasing the acidity of the solution.[37] As expected, the dissociation of complex ions at room temperature is less favoured than at high temperatures, giving rise to a lower degree of supersaturation, and thereby a retarded crystallization process. Therefore, in the RTC process, the crystallization initiation or induction takes a longer time due to a higher critical energy barrier, leading to a larger critical nucleus size (see Table 1). From this stage on, the controlled solvent evaporation provides additional supersaturation to feed a sustainable growth over a period of up to 5 days (Final Stage (III) in Fig. 4b). The experimental data and analysis show that our designed RTC process provides a nearly constant total supersaturation of about 16% for the growth of $MAPbCl_3$ crystals.

Crystal Morphology, Optical Quality, and Ferroelastic Domains. The control of crystallization kinetics and thermodynamics, including thermal conditions and supersaturation, is known to determine the quality of the

grown crystals in terms of crystallinity and transparency.[56-58] The quality of the HT- and RT-grown $MAPbX_3$ (X= Cl and Br) crystals were examined by optical microscopy, which revealed a rough surface with dark spots arising from defects/strains and inclusions on the $MAPbCl_3$ crystal grown by the seeded ITC method (Figure S8a). A much smoother surface with lower strain or inclusions was observed for the RTC-grown crystals of $MAPbCl_3$ and $MAPbBr_3$, as shown in Fig. S8b-c, respectively. The sharp increase in supersaturation at high temperatures can cause an unstable growth that in turn leads to the uneven development of the growing layers, as observed in the HT-grown $MAPbCl_3$ crystals. In particular, the formation of new layers before a previous layer reaches the edge of the crystal due to the unstable growth condition results in the incompletely developed layers and thereby uneven growth steps. As the crystal grows, a sudden decrease in supersaturation occurs due to a high nucleation rate in the ITC process, which facilitates the nucleation in the regions with low surface energy such as the edges or corners of the crystals, and leads to the formation of the raised edges. In contrast, the good transparency and smooth surface of the RTC-grown crystals with less internal strains can be attributed to a more stable growth under a moderate constant supersaturation, leading to more complete layer-by-layer growth at room temperature.

Of note, a number of factors may affect the quality and morphology of the $MAPbX_3$ grown by RTC. For instance, the $MAPbBr_3$ crystals exhibit mixed cuboid and dodecahedral morphologies. This can be explained by the different growth rates along the main crystallographic directions, e.g. $[100]_{cub}$, $[110]_{cub}$ and $[111]_{cub}$, since a cuboid shape results from the fact that the growth rate is the slowest along the $[100]_{cub}$, while a dodecahedron forms when the growth rates are comparable along the three main directions, giving rise to visible $\{100\}_{cub}$, $\{110\}_{cub}$ and/or $\{111\}_{cub}$ facets. The growth conditions are known to affect the crystal morphology. It was reported that a higher X-/PbX_2 ratio may favour the growth of cuboids over dodecahedral morphology.[59] In the RTC method, the formation of complex ions in the $MAPbBr_3$ and $MAPbCl_3$ solutions or evaporation of the CH_3NH_3 ions from the $MAPbI_3$ solution at 45°C may change the solute ratios and consequently affect the quality and morphology of the crystals. On the other hand, the crystal growth rate is determined by the deposition rate of the solute onto the crystal surface and the diffusion rate of the solute in the solution where the deposition rate is controlled by temperature and solution concentration, while the diffusion rate is determined by the concentration gradient of the solution. There must be a balance between the deposition rate and the diffusion rate to grow a high-quality single crystal. In the RTC method, both temperature and concentration of the solution are constant, while the solvent evaporation can affect the concentration of the solution and its gradient. For $MAPbBr_3$ and $MAPbI_3$, the diffusion rate can be higher than the deposition rate because the evaporation rates of DMF and GBL are relatively high, especially GBL at 45°C. This condition creates oversupplied solutes, which can lead to imperfect crystals with twins and scars. Thus, limiting the solute diffusion process could control the crystal growth rate and thereby improve the quality of the grown crystals.The optical transparency of the RTC-grown crystals allows us to observe and analyse their domain structures and crystal symmetry by polarized light microscopy (PLM) in transmission. Figure 5a and 5b shows selected PLM micrographs for X = Cl and X = Br, respectively. Both the $MAPbCl_3$ and $MAPbBr_3$ crystals appear to be dark (in complete extinction) under crossed polarizers ($0° < \delta < 45°$), indicating that they are optically isotropic at room temperature, consistent with the cubic symmetry (α phase) [Fig. 5a(1) & 5b(1)]. Upon cooling, the $MAPbCl_3$ crystal undergoes a phase transition from the cubic to an orthorhombic (β) phase at 178 K with the development of ferroelastic twin domains [Fig. 5a(2)] and then to another orthorhombic (γ) phase at a lower temperature of 172 K [Fig. 5a(3)]. Note that the PLM image of Fig. 5a(2) was taken with a first-order red (FOR) plate (λ = 530 nm) placed between the sample and the analyzer to distinguish the domain walls, which are orientated at the angles of 0/90° and 45°. The analysis of the domain structure and domain wall orientations reveals that the intermediate β phase of $MAPbCl_3$ belongs to the side-centred orthorhombic O_s symmetry,[20] rather than the tetragonal symmetry reported previously.[26] The γ-phase is of primitive orthorhombic O_p symmetry. On the other hand, the $MAPbBr_3$ crystal transforms, upon cooling, from the cubic to a tetragonal phase at 236 K, which appears as a single domain [Fig. 5b(2)], then to an orthorhombic O_s-phase at 152 K [Figure 5b(3)], and finally to another orthorhombic O_s-phase at 148 K [Figure 5b(4)]. More detailed information on the optical crystallography principles used for domain structure and crystal symmetry analysis can be found in our recent work.[20] The characterizations of other structural and physical properties of our crystals, especially for X = Cl, including crystal symmetry and domain configuration, ferroelasticity, Raman spectroscopy, neutron scattering, and dielectric constant also confirm the high quality of the RTC-grown crystals.[20-22, 60]

Absorption, Photoluminescent (PL), and Time-resolved PL Properties. For potential optoelectronic applications, the optical properties of the $MAPbX_3$ crystals were investigated under ambient conditions in terms of absorption and photoluminescence (PL) response. Fig. 6 shows that the crystals exhibit a narrow PL peaks (blue curves) located at 445 nm, 545 nm, and 745 nm for $MAPbCl_3$, $MAPbBr_3$, and $MAPbI_3$, respectively, very close to the values reported previously.[7,18,28] From the steady-state absorption measurements, a sharp band edge is observed at 420 nm, 547 nm and 780 nm for $MAPbCl_3$, $MAPbBr_3$, and $MAPbI_3$, respectively (Fig. 6, pink curves), corresponding to a direct bandgap of 2.50 eV for $MAPbCl_3$, 2.10 eV for $MAPbBr_3$ and 1.47 eV for $MAPbI_3$, which is calculated from the Tauc plots (Insets in Fig. 6). Of note, the $MAPbCl_3$ and $MAPbBr_3$ crystals used for the optical investigation were grown more than two years ago, and their decent optoelectronic behaviour demonstrates the long-term stability of the crystals in terms of physical properties, in addition to the stability of composition, structure, and phase.

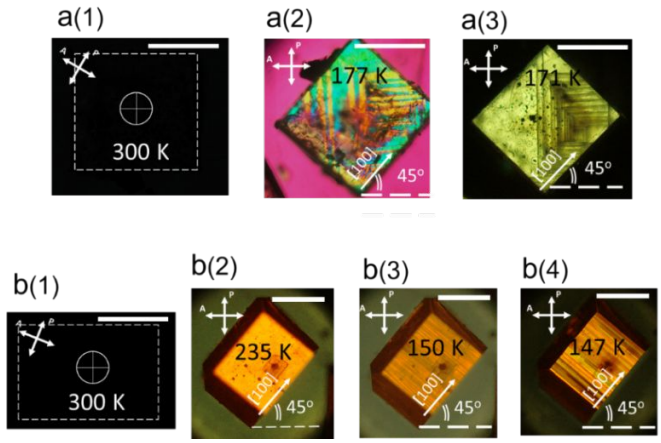

Fig. 5. Optical micrographic images of the (001)-oriented $CH_3NH_3PbX_3$ crystals (a: X = Cl, thickness = 100 µm; B: X = Br; Thickness = 140 µm) obtained by polarized light microscopy in transmission. a(1) and b(1): Both $MAPbCl_3$ and $MAPbBr_3$ crystals appear to be dark (in complete extinction) under crossed polarizers ($0° < \delta < 45°$), indicating that they are optically isotropic at room temperature, consistent with the cubic symmetry (α phase). a(2) and a(3): Ferroelastic twin domains and domain walls developed in the intermediate (β) phase with a side-centred orthorhombic (O_s) phase at 177 K, and in the low-temperature (γ) phase with a primitive orthorhombic (O_p) symmetry at 171K, respectively, of the $MAPbCl_3$ crystal; a(2) was taken with a first-order red plate (λ = 530 nm) inserted between the crystal and the analyzer. b (2): Single domain state in the tetragonal (β) phase of the $MAPbBr_3$ crystal at 235 K. b(3) and b(4): Ferroelastic twin domains and domain walls developed in the intermediate (β') phase with a side-centred orthorhombic (O_s) symmetry at 150 K, and in the low-temperature (γ) phase also with a side-centred orthorhombic (O_s) symmetry at 147 K, respectively, of the $MAPbBr_3$ crystal. Note: The PLM pictures of a (2-3) and b (2-4) were taken with the [100]-direction of the crystals oriented at an angle of 45° to the directions of the crossed polarizers. The temperature, crystallographic directions and polarizer/analyzer directions are indicated. Scale bars: 200 µm.

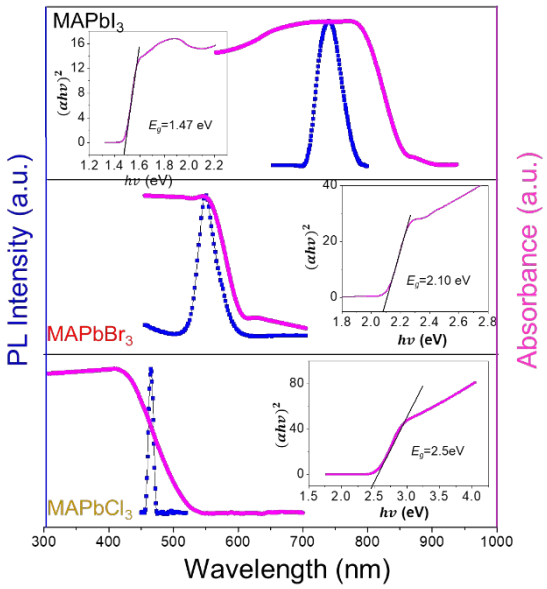

Fig. 6 Absorption and steady-state photoluminescence spectra of the $MAPbX_3$ (X = I, Br and Cl) single crystals grown by RTC. Insets show the determination of optical band gap using the Tauc plots.

Time-resolved photoluminescence (PL) spectra were acquired using the time-correlated single photon counting (TCSPC) setup to investigate the dynamics of exciton recombination in the $MAPbBr_3$ and $MAPbI_3$ crystals. The PL spectra were fit with a four-exponential decay, as shown in Fig. 7. Very short-lived components $\tau_1 \approx 0.35$ ns and ≈ 0.15 ns were observed for the $MAPbBr_3$ and $MAPbI_3$ crystals, respectively, which were limited by the instrument response of TCSPC. The PL decay times of both crystals measured under ambient conditions showed a short-lived PL lifetime (τ_2), long-lived PL lifetime (τ_3) and ultralong-lived component (τ_4), as shown in Table S1. A relatively large contribution of the longer PL lifetimes indicates the good optical properties of the crystals compared to the PL decay lifetimes of the previously reported ITC crystals.[61,62,63] Remarkably, the crystals grown recently (the fresh crystals), and the crystals grown two years ago for $MAPbBr_3$ and six months ago for $MAPbI_3$ (the old crystals) showed similar PL lifetime properties, indicating a good long-term stability of the RTC-grown crystals. In particular, the τ_4 values in $MAPbBr_3$ with ~ 48% of the total PL contribution are 115 ns and 153 ns for the old and fresh crystals, respectively, and the τ_4 values in $MAPbI_3$ with ~ 36% of the total PL contribution are 111 ns and 117 ns for the old and fresh crystals, respectively.

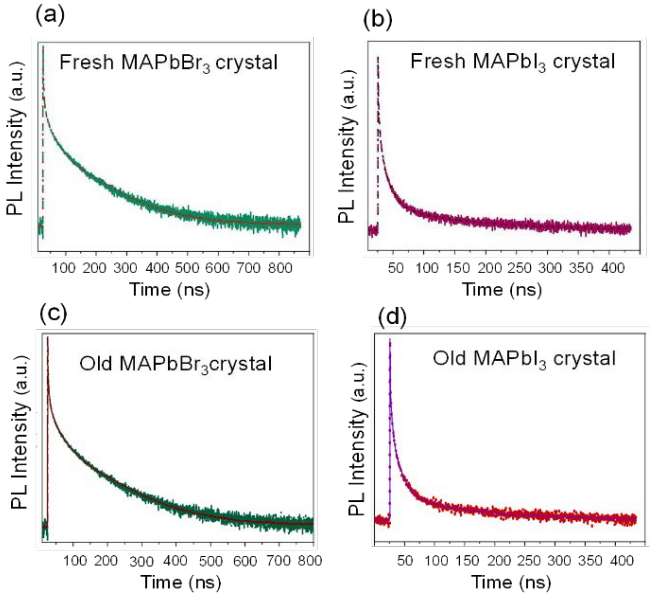

Fig. 7 Time-resolved PL spectra of the fresh RTC-grown crystals of (a) $MAPbBr_3$ and (b) $MAPbI_3$, and of the old RTC-grown crystals of (c) $MAPbBr_3$ and (d) $MAPbI_3$.

We have characterized the charge-transport properties of $MAPbX_3$ (X= I, Br, Cl) crystals, including the trap density and (hole) carrier mobility from the dark current-voltage (*J-V*) characteristics, using the standard space charge-limited current (SCLC) model. As shown in Fig. 8, the *J-V* relation exhibits the Mott-Gurney's power-law dependence, where an Ohmic behaviour ($J \propto V$) is observed at low voltages. By increasing the voltage above the trap-filled limited voltage (V_{TFL}), a sharp increase in the current is found with a non-linear behaviour ($J \propto V^{n>3}$). This is an indication of the trap-filled limit (TFL) process, in which the trap states are filled by the charge carriers. The trap density (n_{trap}) can be determined using the following equation:

$$V_{TFL} = \frac{en_{trap}L^2}{2\varepsilon\varepsilon_0}, \quad (3)$$

where e is the elementary charge, L is the thickness of the crystal, ε_0 is vacuum permittivity, and ε is the dielectric constant (≈ 25.5 for $MAPbX_3$ (X= I, Br) and 23.9 for $MAPbCl_3$).[26] From Equation 3, the values of trap density n_{trap} are calculated to be 1.36x10^{10} cm^{-3} for $MAPbI_3$, 2.06x10^{10} cm^{-3} for $MAPbBr_3$, and 4.27x10^{9} cm^{-3} for $MAPbCl_3$ and the V_{TFL} values are extracted from the *J-V* characteristics, as indicated in Fig. 8a-c. At higher voltage (the Child region), the current shows a quadratic dependence on voltage ($J \propto V^2$) and the relation can be stated as:

$$J_D = \frac{9\varepsilon\varepsilon_0\mu V^2}{8L^3}, \quad (4)$$

where J_D, V, and μ are the current density, the applied voltage, and the hole carrier mobility, respectively. According to Equation 4, the carrier mobility values are calculated to be ~ 410 cm^{2}V^{-1}s^{-1} for $MAPbI_3$, 47 cm^{2}V^{-1}s^{-1} for $MAPbBr_3$, and 12 cm^{2}V^{-1}s^{-1} for $MAPbCl_3$. Furthermore, having the carrier lifetime (τ) and mobility (μ), one can calculate the carrier diffusion length (L_D) of the crystals from the following equation:

$$L_D = \sqrt{\frac{\mu\tau k_\beta T}{e}}, \quad (5)$$

where K_B is the Boltzman constant, and T is the temperature. The L_D values of the crystals are calculated to be 10.75 µm for $MAPbI_3$ and 3.72 µm for $MAPbBr_3$ for a long recombination time (~110 ns). Therefore, the charge-transport characteristics and trap densities obtained for the RTC-grown crystals are comparable to those of the single crystals grown by the other methods.[7,18,28,38] In particular, the RTC-grown $MAPbI_3$ crystal exhibits an ultra-high carrier mobility μ of 410 cm^{2}V^{-1}s^{-1} and an ultra-long diffusion length L_D of 10.75 µm, suggesting that it could be a promising material for high-performance optoelectronic devices. To the best of our knowledge, this is the first report on the long-term carrier properties of the halide perovskite single crystals.

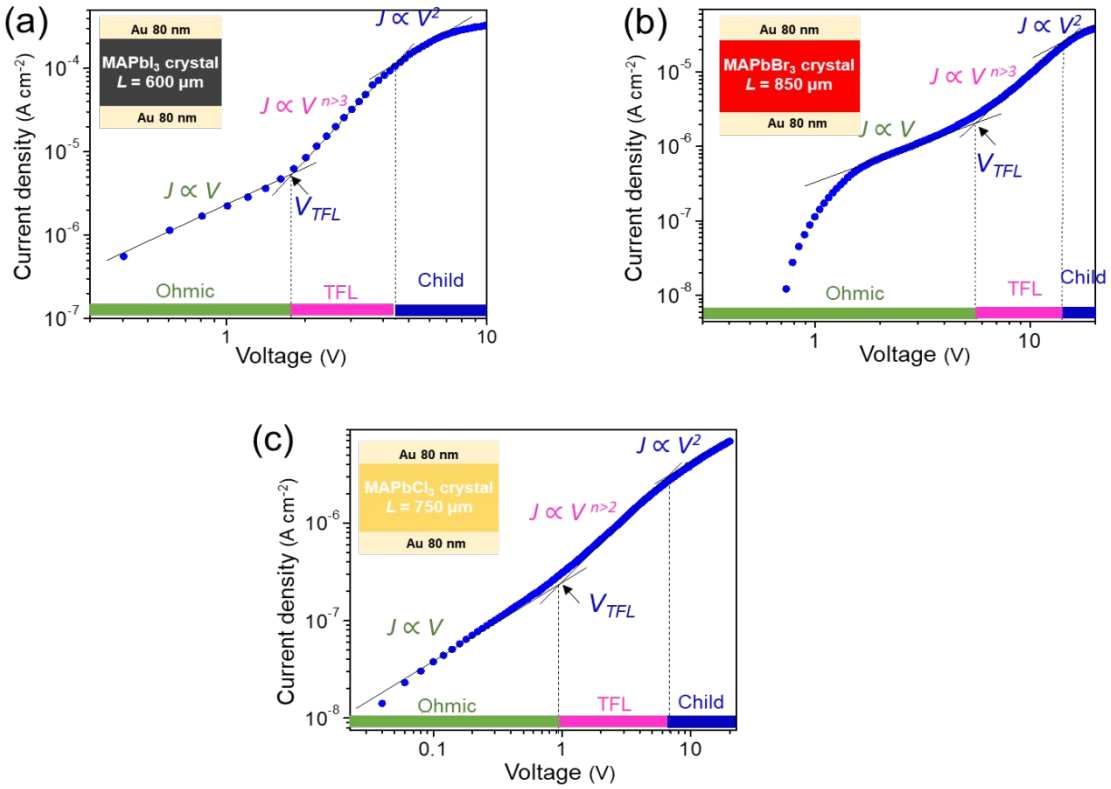

Fig. 8. Characteristic current-voltage (*J-V*) curves of the RTC-grown $CH_3NH_3PbX_3$ crystals, (a) $CH_3NH_3PbI_3$, (b) $CH_3NH_3PbBr_3$, (c) $CH_3NH_3PbCl_3$, exhibiting three different regions, corresponding to the Ohmic, trap filling limit (TFL), and Child, as shown by different colours.

Experimental

All chemicals and reagents were purchased from Sigma-Aldrich and used as received without further treatment.

Growth of $MAPbX_3$ (X= I, Br and Cl) single crystals by the RTC method. A homogenous saturated solution was first prepared by continuous stirring at 60 °C (except for X=Br at room temperature) for two hours. Specifically, 1.6 g of methylammonium iodine (> 98%) and 4.6 g of lead(II) iodide (> 99%) were dissolved in 10 mL GBL solvent for X= I, 1.7 g of methylammonium bromide (> 98%) and 5.5 g of lead(II) bromide (> 99%) were dissolved in 10 mL DMF solvent for X= Br, 1.4 g of methylammonium chloride (> 98%) and 5.6 g of lead(II) chloride (> 99%) were dissolved in 10 mL DMSO solvent for X= Cl. In the next step, the solutions were cooled down to room temperature (20 to 25 °C) for of X= Br, Cl, or to 45 °C for X= I and then transferred into a 50 % closed, partially capped vial for X= Br, Cl, and into a 100 % open vial for X= I, and then kept therein at these temperatures. As shown in Fig. S1, many $MAPbI_3$, $MAPbBr_3$, and $MAPbCl_3$ single crystals were grown after 6, 12 hours, and 5 days, respectively.

Growth of $CH_3NH_3PbCl_3$ crystals by the seed-assisted ITC method. Stoichiometric amounts of chloride precursors, i.e., 1.4 g of methylammonium chloride (> 98%) and 5.6 g of lead chloride (> 99%), were dissolved into 10 mL DMSO solvent by continuous stirring on a heating plate at 60 °C for two hours. The solution was poured into a vial, which was then fully sealed, and heated from 60 °C to 110 °C in a mineral oil bath. The sealed vial remained at the temperature of 110 °C in the undisturbed mineral oil bath for the single crystals to grow. After 12 hours of growth, single crystals of various sizes were obtained in the vial. A crystal of high quality was selected to serve as the seed for the second round of growth by seed–assisted ITC. The seed was placed into a fresh solution, heated to, and kept at, 110 °C for 12 hours. The original 2 mm^3 seed was grown into a larger one in the second run (Fig. 1d).

Powder & single-crystal X-ray diffraction (XRD): Powder X-ray diffraction (PXRD) patterns were obtained using a Rigaku diffractometer equipped with the Cu Kα radiation (λ = 1.5405Å). Powders of $MAPbX_3$ (X= I, Br and Cl) and intermediate compounds of X=Cl and I were prepared by grinding large crystals into fine powders. A yellow layer formed on the $MAPbI_3$ crystal was scratched out for XRD analysis. The MACl and $PbCl_2$ powders were also analyzed as references. The resultant diffraction data were collected for Pawley structural analysis and refinement of lattice parameters by using TOPAS software package. A Bruker D8 Advance Diffractometer equipped with a Goebel mirror for a parallel X-ray beam for high-resolution diffraction was used to perform single-crystal X-ray diffraction of $MAPbX_3$ (X= I, Br. Cl) crystals grown by RTC.

Energy-dispersive X-ray spectroscopy (EDX) and Infrared spectroscopy (IR) measurements: The chemical composition of the $CH_3NH_3PbX_3$ crystals prepared by RTC was determined by using a FEI Nova NanoSEM 430 system equipped with an EDX spectrometer. The infrared spectroscopy measurement was carried out in the wave number range of 4000 - 500 cm^{-1} on both pure $CH_3NH_3PbCl_3$ and the intermediate compound formed by the RTC method and the data were recorded on a Spectrum Two FT-IR spectrophotometer at room temperature.

Solubility and supersaturation characterizations: The solubility behaviour of $CH_3NH_3PbX_3$ in polar solvents was studied by changing the temperature of the solution from 25 °C to 120 °C with a step of 10 °C. At each given temperature, 0.2 g of $CH_3NH_3PbX_3$ powder prepared by heating the precursor solution to 60 °C to evaporate the solvent, was added into 20 mL of solvent step-by-step and the solution was continuously stirred until the chemicals were dissolved completely in the solvent. The solution was considered to have reached saturation when the $CH_3NH_3PbX_3$ powder could no longer dissolve in the solvent upon the further addition of the solute. The solubility is described by the equilibrium concentration (C^*) at a given temperature, and C^* is the ratio of the mass of the dissolved $MAPbX_3$ powder to the volume (mL) of the solvent. The supersaturation arising from solubility reduction is defined as:

$$S_{sr} = \frac{|C^*_{final} - C^*_{initial}|}{C^*_{initail}} \times 100, \quad (6)$$

where C^*_{final} and $C^*_{initial}$ are the equilibrium concentration at growth temperature, and the equilibrium concentration at which the precursor solution is first prepared, respectively.

The supersaturation of solvent evaporation for RTC was obtained from the equation:

$$S_{se} = \frac{\left(\frac{m_{initial}}{V_{sol}(t)}\right) - C^*_{initial}}{C^*_{initial}} \times 100, \quad (7)$$

where m initial is the initial mass of powder dissolved in the solvent (6.2 g for X=I, 7.2 g for X=Br and 7 g for X=Cl), , $V_{sol}(t)$ is the volume of solvent used in our experiment which was 10 mL at t = 0 and it varies with the time (t). The decrease in supersaturation due to crystal growth is obtained from the equation:

$$S_{cg} = \frac{\left(\frac{m_{initial} - m_{grown\ crystals}}{V_{sol}}\right) - C^*_{initial}}{C^*_{initial}} \times 100 \quad (8)$$

where $m_{grown\ crystals}$ is the mass of the grown crystals and were calculated from the relation of $m_{grown\ crystals} = \rho_{MAPbX3} \times V_{crystals}$, where the density (ρ) of $MAPbX_3$ is 0.00312 g mm^{-3}, 0.00383g mm^{-3} and 0.00417 g mm^{-3} for X= Cl, Br, and I, respectively,[25] and the volume ($V_{crystals}$) of crystals was recorded during growth. Fig. 2 shows the average values of the solubility and supersaturation for $MAPbX_3$ during these measurements.

Induction period measurement. The induction period was measured experimentally at different supersaturation ratios ($S_r = C/C^*$) for two temperatures: 25 °C and 110°C. First, the saturated solution was prepared at different temperatures according to the solubility values. Then, the solution was heated to 110 °C to obtain a desired supersaturation. The supersaturated solution was held isothermally at 110 °C until

the first crystal nuclei were observed. The time taken for the first crystal to appear from the supersaturated solution was recorded as the induction time. The same procedure was carried out to obtain induction time at 25 °C for different supersaturation ratios.

Optical characterization of $MAPbX_3$ single crystals. The surface roughness and morphology of the grown $CH_3NH_3PbX_3$ were examined by optical microscopy. The crystallographic orientation of the crystals was confirmed using SC diffraction, as shown in Fig. 1f-g, which confirmed that the naturally grown facets are the $\{100\}_{cub}$ faces. The domain structure and phase transitions of the RTC-grown $CH_3NH_3PbCl_3$ (~0.10 mm thick) and $CH_3NH_3PbBr_3$ (~0.12 mm thick) crystal platelets were investigated by polarized light microscopy (PLM) in transmission, using an Olympus BX60 polarizing microscope equipped with an Olympus UC 30 digital camera and a first order red (FOR) plate (530 nm). A Linkam HTMS600 heating/cooling stage was used for investigating the variations of domain structures and phase transitions in the temperature range of 80 K to 300 K at a heating and cooling rate of ~2 K min^{-1}.

Absorption, steady-state photoluminescence (PL), and Time-resolved PL measurements. The optical absorption spectra of the crystals were measured using an Ocean Optics Flame Spectrometer. The excitation was achieved using a DH-2000 light source equipped with both a deuterium and a halogen lamp passed through a Thorlabs bandpass optical filter. The steady-state photoluminescence measurements were carried out using a Photon Technology International (PTI) QuantaMaster spectrofluorometer. The time-resolved PL spectra were collected on a Horiba PTI spectrometer with a DeltaFlex time-correlated single photon counting (TCSPC) lifetime measurement system equipped with a 370 nm excitation laser pulse.

Space charge limited current (SCLC) measurement. The variation of current as a function of the voltage was measured using a Keithley 2401 source meter in the dark at room temperature. Hole-only devices were prepared by sputter-deposition of 80 nm gold layers on opposite sides of the crystals as electrodes with the surface areas of 2x1.1 mm^2 for $MAPbI_3$, 2x1.7 mm^2 for $MAPbBr_3$, and 1.7x1.7 mm^2 for $MAPbCl_3$. The *J-V* response was analysed based on the SCLC model.

Conclusions

An optimized room-temperature crystallization (RTC) process is designed upon examination of solubility behaviour, and successfully applied for the growth of organic-inorganic hybrid halide perovskite $MAPbX_3$ (X = I, Br and Cl) crystals from polar solvents with the aid of solvent evaporation. The crystals grown by RTC are comparatively large and transparent (except for the X = I ones which are opaque) with a regular cubic morphology. This growth process results in high yields (~40 wt%, 60 wt%, and 15% for the I, Br, and Cl-based perovskites, respectively). The optimum supersaturation (S_{total}) for a stable RT growth of $MAPbX_3$ crystals is found to be 12%, 13%, and 16% for X= I, Br, and Cl, respectively, from the assessment of the supersaturation components from solubility reduction (S_{sr}), solvent evaporation (S_{se}) and grown crystal quantity (S_{cg}). Based on classical nucleation theory, the nucleation parameters such as interfacial energies, critical nuclei radius, critical free energy barrier, and volume free energy change were calculated and compared for the crystal growth via RT and high temperature (HT) processes, which gives a deep insight into the nucleation processes. The small interfacial energy of HT growth results in a high nucleation rate, causing an abrupt decrease in supersaturation and preventing further crystal growth after a few hours. In contrast, the RTC method provides a relatively large interfacial energy and a longer induction time due to the slow dissociation of complex ions, resulting in a decreased nucleation rate, a retarded crystallization process, and a more stable and sustainable growth. The controlled evaporation in the RTC process helps achieve a constant supersaturation during the crystal growth and allows the crystals to grow continuously into a large size.

The polarized light microscopic studies reveal ferroelastic twin domains and domain walls characteristic of the orthorhombic and tetragonal phases of the $MAPbCl_3$ and $MAPbBr_3$ crystals, respectively. The absorption and photoluminescence, and charge-transport properties indicate excellent optoelectronic properties of the RTC-grown $MAPbX_3$ crystals. Of note, the crystals of X = Br and Cl demonstrate an excellent long-term (> two years) stability in terms of composition, structure, phase, and optoelectronic properties. Our investigation shows that the size and optical quality of the crystals can be controlled by temperature and supersaturation and the optimum thermodynamic and kinetic conditions attained in the RTC method are advantageous over the HT process. The RTC growth method developed in this work can be scaled up for cost-effective mass production of high-quality $MAPbX_3$ crystals, which will promote not only more in-depth investigations into the intrinsic optical, electrical properties of hybrid halide perovskites, but also the realization of single crystals-based optoelectronic devices of superior performance.

Conflicts of interest

There are no conflicts to declare.

Acknowledgments

This work was supported by the Natural Sciences and Engineering Research Council of Canada (NSERC, Grant Nos. RGPIN-2017-06915, and RGPIN-2020-06522) and the U. S. Office of Naval Research (ONR, Grant No. N00014-16-1-3106).

Notes and references

1 M. A. Green, A. Ho-Baillie, H. J. Snaith, *Nat. Photonics* 2014, **8**, 506-514.

2 Z. K. Tan, R. S. Moghaddam, M. L. Lai, P. Docampo, R. Higler, F. Deschler, M. Price, A. Sadhanala, L. M. Pazos, D.

Credgington, F. Hanusch, T. Bein, H. J. Snaith, R. H. Friend, *Nat. Nanotechnol.* 2014, **9**, 687-692.
3 Y. Guo, C. Liu, H. Tanaka, E. Nakamura, *J. Phys. Chem. Lett.* 2015, **6**, 535-539.
4 G. Xing, N. Mathews, S. S. Lim, N. Yantara, X. Liu, D. Sabba, M. Gratzel, S. Mhaisalkar, T. C. Sum, *Nat. Mater.* 2014, **13**, 476-480.
5 W. S. Yang, J. H. Noh, N. J. Jeon, Y. C. Kim, S. Ryu, J. Seo, S. Seok, *Science* 2015, **348**, 1234-1237.
6 M. Cao, J. Tian, Z. Cai, L. Peng, L. Yang, D. Wei, *Appl. Phys. Lett.* 2016, **109**, 233303.
7 G. Maculan, A. D. Sheikh, A. L. Abdelhady, M. I. Saidaminov, M. A. Haque, B. Murali, E. Alarousu, O. F. Mohammed, T. Wu, O. M. Bakr, *J. Phys. Chem. Lett.* 2015, **6**, 3781-3786.
8 Y. Fang, Q. Dong, Y. Shao, Y. Yuan, J. Huang, *Nat. Photonics* 2015, **9**, 679-686.
9 J. Yang, K. Liu, Z. Cheng, P. Jing, Q. Ai, X. Chen, B. Li, Z. Zhang, L. Zhang, H. Zhao, D. Shen, *ACS Appl. Mater. Interfaces* 2018, **10**, 34744-34750.
10 H. Wei, Y. Fang, P. Mulligan, W. Chuirazzi, H.-H. Fang, C. Wang, B. R. Ecker, Y. Gao, M. A. Loi, L. Cao, J. Huang, *Nat. Photonics* 2016, **10**, 333-340.
11 S. Yakunin, D. N. Dirin, Y. Shynkarenko, V. Morad, I. Cherniukh, O. Nazarenko, D. Kreil, T. Nauser, M. V. Kovalenko, *Nat. Photonics* 2016, **10**, 585-589.
12 T.-C. Wei, S. Mokkapati, T.-Y. Li, C.-H. Lin, G.-R. Lin, C. Jagadish, J.-H. He, *Adv. Funct. Mater.* 2018, **28**, 1707175.
13 G. Walters, B. R. Sutherland, S. Hoogland, D. Shi, R. Comin, D. P. Sellan, O. M. Baker, E. H. Sargent, *ACS Nano* 2015, **9**, 9340-9346.
14 J. Leuthold, C. Koos, W. Freude, *Nat. Photonics* 2010, **4**, 535-544.
15 M. Razeghi, A. Rogalski, *J. Appl. Phys.* 1996, **79**, 7433-7473.
16 Y. Liu, Y. Zhang, K. Zhao, Z. Yang, J. Feng, X. Zhang, K. Wang, L. Meng, H. Ye, M. Liu, S. F. Liu, *Adv. Mater*. 2018, **30**, 1707314.
17 B. Chen, T. Li, Q. Dong, E. Mosconi, J. Song, Z. Chen, Y. Deng, Y. Liu, S. Ducharme, A. Gruverman, F. Angelis, J. Huang, *Nat. Mater.* 2018, **17**, 1020-1026.
18 D. Shi, V. Adinolfi, R. Comin, M. Yuan, E. Alarousu, A. Buin, Y. Chen, S. Hoogland, A. Rothenberger, K. Katsiev, Y. Losovyj, X. Zhang, P. A. Dowben, O. F. Mohammed, E. H. Sargent, O. M. Bakr, *Science* 2015, **347**, 519-522.
19 Y. Yang, Y. Yan, M. Yang, S. Choi, K. Zhu, J. M. Luther, M. C. Beard, *Nat. Commun*. 2015, 6, 7961.
20 M. Bari, A. A. Bokov, Z.-G. Ye, *J. Mater. Chem. C* 2020, **8**, 9625-9631.
21 T. T. Nguyen, Y. Kim, S. Bae, M. Bari. H. R. Jung, W. Jo, Y.-H. Kim, Z. -G. Ye, S. Yoon, *J. Phys. Chem. Lett.* 2020, **11**, 3773–3781.
22 M. Songvilay, M. Bari, Z.-G. Ye, G. Xu, P. M. Gehring, W. D. Ratcliff, K. Schmalzl, F. Bourdarot, B. Roessli, C. Stock, *Phys. Rev. Mater*.2018, **2**, 123601.
23 E. Strelcov, Q. Dong, T. Li, J. Chae, Y. Shao Y. Deng, A. Gruverman, J. Huang, A. Centrone, *Sci. Adv.* 2017, **3**, 1602165.
24 Yin, W. J.; Shi, T.; Yan, Y. *Adv. Mater*. 2014, **26**, 4653-4658.
25 D. Weber, *Z. Naturforsch. B*, 1978, **33**, 1443-1445.
26 A. Poglitsch, D. Weber, *J. Chem. Phys.* 1987, **87**, 6373-6378.
27 M. Maeda, M. Hattori, A. Hotta, I. Suzuki, *J. Phys. Soc. Jpn.* 1997, **66**, 1508-1511.
28 M. I. Saidaminov, A. L. Abdelhady, B. Murali, E. Alarousu, V. M. Burlakov, W. Peng, I. Dursun, L. Wang, Y. He, G. Maculan, A. Goriely, T.; Wu, O. F. Mohammed, O. M. Bakr, *Nat. Commun*. 2015, **6**, 7586.
29 J. M. Kadro, K. Nonomura, D. Gachet, M. Gratzel, A. Hagfeldt, *Sci. Rep.* 2015, **5**, 11654.
30 Y. Dang, Y. Liu, Y. Sun, D. Yuan, X. Liu, W. Lu, G. Liu, H. Xia, X. Tao, *CrystEngComm.* 2015, **17**, 665-670.
31 Z. Lian, Q. Yan, Q. Lv, Y. Wang, L. Liu, L. Zhang, S. Pan, Q. Li, L. Wang, J. L. Sun, *Sci. Rep.* 2015, **5**, 16563.
32 Y. Dang, Y. Zhou, X. Liu, D. Ju, S. Xia, H. Xia, X. Tao, *Angew. Chem. Int. Ed. Engl.* 2016, **55**, 3447-3450.
33 Y. Liu, Z. Yang, D. Cui, X. Ren, J. Sun, X. Liu, J. Zhang, Q. Wei, H. Fan, F. Yu, X. Zhang, C. Zhao, S. F. Liu, *Adv. Mater*. 2015, **27**, 5176-5183.
34 Z. Chen, B. Turedi, A. Y. Alsalloum, C. Yang, X. Zheng, I. Gereige, A. AlSaggaf, O. F. Mohammed, O. M. Bakr, *ACS Energy Lett.* 2019, **4**, 1258-1259.
35 H. S. Rao, W. G. Li, B. X. Chen, D. B. Kuang, C. Y. Su, *Adv. Mater.* 2017, **29**, 1602639.
36 Y. Liu, Y. Zhang, Z. Yang, J. Feng, Z. Xu, Q. Li, M. Hu, H. Ye, X. Zhang, M. Liu, K. Zhao, S. Liu, *Mater. Today* 2019, **22**, 67-75.
37 P. K. Nayak,; D. T. Moore,; B. Wenger,; S. Nayak,; A. A. Haghighirad, A. Fineberg, N. K. Noel, O. G. Reid, G. Rumbles, P. Kukura, K. A. Vincent, H. J. Snaith, *Nat. Commun.* 2016, **7**, 13303.
38 F. Yao, J. Peng, R. Li, W. Li, P. Gui, B. Li, C. Liu, C. Tao, Q. Lin, G. Fang, *Nat. Commun.* 2020, **11**, 1194.
39 P. Nandi, C. Giri, D. Swain, U. Manju, D. Topwal, *CrystEngComm.* 2019, **21**, 656-661.
40 R. Gupta, T. B. Korukonda, S. K. Gupta, B. P. Dhamaniy, P. Chhillar, R. Datt, P. Vashishtha, G. Gupta, V. Gupta, R. Srivastava, S. Pathak, *J. Cryst. Growth.* 2020, **537**, 125598.
41 Y. Wu, A. Islam, X. Yang, C. Qin, J. Liu, K. Zhang, W. Peng, L. Han, *Energy Environ. Sci.* 2014, **7**, 2934-2938.
42 F. Hao, C. C. Stoumpos, P. Guo, N. Zhou, T. J. Marks, R. P. Chang, M. G. Kanatzidis, *J. Am. Chem. Soc.* 2015, **137**, 11445-11452.
43 Y. Liu, X. Ren, J. Zhang, Z. Yang, D. Yang, F. Yu, J. Sun, C. Zhao, Z. Yao, B. Wang, Q. Wei, F. Xiao, H. Fan, H. Deng, L. Deng, S. Liu, *Sci. China Chem. 2017*, **60**, 1367-1376.
44 J. A. Christians, P. A. Miranda Herrera, P. V. Kamat, *J. Am. Chem. Soc.* 2015, **137**, 1530-1538.
45 S. A. Fateev, A. A. Petrov, V. N. Khrustalev, P. V. Dorovatovskii, Y. V. Zubavichus, E. A. Goodilin, A. B. Tarasov, *Chem. Mater*. 2018, **30**, 5237−5244.
46 D. Elwell, and H. J. Scheel, *Crystal Growth from High-Temperature Solutions*, Academic Press Inc, London - New York, 1975.
47 N. P. Zaitseva, L.N. Rashkovich, S. V. Bogatyreva. *J. Cryst. Growth*. 1995, **148**, 276-282.
48 M. Lenka, D. Sarkar, *J. Cryst. Growth* 2014, **408**, 85-90.
49 A. Kuldipkumar, G. S. Kwon, G. G. Z. Zhang, *Cryst. Growth Des.* 2007, **7**, 232-242.
50 N. J. Jeon, J. H. Noh, Y. C. Kim, W. S. Yang, S. Ryu, S. I. Seok, *Nat. Mater.* 2014, **13**, 897-903.
51 J. S. Manser, B. Reid, P. V. Kamat, *J. Phys. Chem. C* 2015, **119**, 17065-17073.
52 A. A. Zhumekenov, V. M. Burlakov, M. I. Saidaminov, A. Alofi, M. A. Haque, B. Turedi, B. Davaasuren, I. Dursun, N. Cho, A. M. El-Zohry, M. D. Bastiani, A. Giugni, B. Torre, E. D.Fabrizio, O. F. Mohammed, A. Rothenberger, T. Wu, A. Goriely, O. M. Bakr, *ACS Energy Lett.* 2017, **2**, 1782-1788.
53 Y. Rong, S. Venkatesan, R. Guo, Y. Wang, J. Bao, W. Li, Z. Fan, Y. Yao, *Nanoscale* 2016, **8**, 12892-12899.
54 I. Wharf, T. R. Gramstad, M. O. Makhija, *Can. J. Chem.* 1976, **54**, 3430-3438.
55 L. H. Holmes, *Physical Chemical Studies on Inorganic Coordination Compounds. I. Metallic Complexes of Dimethylsulfoxide. II. Preparation and Spectral Studies of Vanadyl Complexes.* LSU Historical Dissertations and Theses. 713, 1961.
56 J. Ding, Y. Zhao, S. Du, Y. Sun, H. Cui, X. Zhan, X. Cheng, L. Jing, *J. Mater. Sci.* 2017, **52**, 7907–7916.

57 S. Amari, J.-M. Verilhac, E. G. D'Aillon, A. Ibanez, J. Zaccaro, *Cryst. Growth Des.* 2020, **20**, 1665–1672.
58 H. Shen, R. Nan, Z. Jian, and X. Li, *J. Mater. Sci.* 2019, **54**, 11596–11603.
59 Y. Zhang, F. Huang, and Q. Mi, *Chem. Lett.* 2016, **45**, 1030-1032.
60 M. Songvilay, N. Giles-Donovan, M. Bari, Z.-G. Ye, J. L. Minns, M. A. Green, Guangyong Xu, P. M. Gehring, K. Schmalzl, W. D. Ratcliff, C. M. Brown, D. Chernyshov, W. van Beek, S. Cochran, and C. Stock, *Phys. Rev. Mater.* 2019, **3**, 093602.
61 B. Wu, H. T. Nguyen, Z. Ku, G. Han, D. Giovanni, N. Mathews, H. J. Fan, and T. C. Sum, *Adv. Energy Mater*. 2016, **6**, 1600551.
62 T. Yamada, Y. Yamada, H. Nishimura, Y. Nakaike, A. Wakamiya, Y. Murata, and Y. Kanemitsu, *Adv. Electron. Mater.* 2016, **2**, 1500290.
63 K.-H. Wang, L.-C. Li, M. Shellaiah, and K. W. Sun, *Sci. Rep* 2017, **7**, 13643.